



Spatial power profiling method using visual information in reactors with optically transparent coolants

Jason A. Hearne^{*}, Pavel V. Tsvetkov

Texas A&M University, United States

ARTICLE INFO

Article history:

Received 30 May 2019

Received in revised form 9 September 2019

Accepted 17 September 2019

Available online 8 October 2019

Keywords:

Reactor instrumentation

Power profile

Cerenkov radiation

Flux mapping

TRIGA

ABSTRACT

The purpose of this study is to develop a method of power profile reconstruction based on visual instrumentation in nuclear reactors with optically transparent coolants. The detection of visible light produced by Cerenkov radiation at points outside of the active core region of a TRIGA reactor is correlated to the spatial power profile within the reactor core using a response function. A detailed MCNP model of the core is used to tally electron fluxes within coolant channels, which then use the response function to produce a 2D map of the Cerenkov radiation above the core. The potential use for this method is demonstrated by modelling various reactor perturbations at constant core power and showing the ability of the method to provide information about what change occurred. Some analysis of the applicability of this method to different reactor designs is performed, with recommendations as to where and how it could be implemented.

© 2019 Elsevier Ltd. All rights reserved.

1. Introduction

The goal of this research effort is to develop a power profile reconstruction method that will enable the application of novel forms of instrumentation in reactors with optically transparent coolants to increase the diversity of instrumentation systems and to provide additional information about the reactor. For example, light water and non-fuel molten salt environments of Light Water Reactors (LWRs) and Fluoride salt cooled High Temperature Reactors (FHRs) offer such conditions. In the present study, the TRIGA (Training, Research, Isotopes, General Atomics) research reactor environment at the Texas A&M Nuclear Science Center (NSC) has been used as a representative reactor configuration. This method aims to provide a way to characterize not only the total power of a reactor, but also the spatial power profile with a non-invasive system to enable higher resolution power mapping. To develop this instrumentation method, a system that uses visual detectors to measure Cerenkov fluxes in a TRIGA reactor is designed. Various different reactor states are modeled to obtain power profiles for the reactor using visual instrumentation to demonstrate the reconstruction method's ability to distinguish between different reactor states.

Currently reactor power instrumentation is primarily done using in core gamma or neutron detectors, or using temperature

sensors (Knoll, 2010; Loving, 1970; Forster, 1965). Many instrumentation methods measure a small number of locations in or near the core to obtain the total core power. Some next generation reactor designs require improved power profile determination (Holcomb et al., 2018). Higher precision spatial power profile measurements could also be used for code validation, xenon oscillation detection, or optimizing fuel loading and burnup.

A few systems that use Cerenkov radiation for power measurement have been designed (Rippon, 1963; Arkani and Gharib, 2007; Arkani and Gharib, 2009; Lovvorn, Oct. 1961; Bentoumi et al., April 2018; Weiss, 1965). It has been shown that in a reactor operating in the intermediate to full power range, the Cerenkov fluxes are proportional to the total power. This has been used in the Tehran Research reactor to measure the total core power to provide another diverse and redundant power measurement system for reactor safety and operations (Arkani and Gharib, 2007). Another system that uses Cerenkov based reactor power measurements to measure reactor kinetic parameters in a pulsing TRIGA reactor for safeguards applications has also been developed (Holschuch and Marcum, 2019). Another type of Cerenkov based flux detector design involves using a small-bore metallic tube to transfer Cerenkov light produced in a small quartz crystal placed within the reactor to a detector (Bentoumi et al., April 2018). This design uses the reflective, empty tube to efficiently transmit the light to the detector, but is limited by the fact that the tube must be present for each location measured. Additionally the high efficiency of light transfer is not necessary for Cerenkov detection in an operating reactor due to the large amount of light generated by the strong gamma fields.

^{*} Corresponding author.

E-mail addresses: jasonhearn@tamu.edu (J.A. Hearne), tsvetkov@tamu.edu (P.V. Tsvetkov).

Another similar existing technology is the use of Cerenkov detection in safeguards to verify the burnup of spent fuel assemblies. The Improved Cerenkov Viewing Device (ICVD) and Digital Cerenkov Viewing Device (DCVD) are used by the IAEA to verify the declared burnup of spent fuel assemblies and to ensure that fuel has not been diverted and replaced with non-fuel materials (Safeguards Techniques and Equipment, 2011). This method performs a 2d spatial mapping of the Cerenkov flux generated by an assembly due to decay and therefore shares similarities with the goal of reactor power profiling. Data collection with the ICVD used in safeguards is generally done by hand in a spent fuel pool rather than by an automated system for an operating reactor. The ICVD is detecting the Cerenkov flux from a static system with gamma emission from radioactive decay as the ultimate source of the Cerenkov production, and the detection goal is the ability to determine whether or not a given assembly has the correct burnup and that no pins have been covertly removed or replaced. The ICVD has some issues with low light levels caused by the spent fuel not producing enough Cerenkov radiation for the detector. Problems with an insufficient light level are not present in an operating reactor, as the gamma field strength and thus Cerenkov production is much greater.

Visual instrumentation is commonly used for refueling and inspection during reactor outages (Farley and "An, 2004, 2004.). An example of the ability to see Cerenkov radiation coming from decay gammas in coolant channels within a BWR during a refueling outage is publicly available in a demonstration of a refueling machine camera (Refueling, 2012). While an interesting demonstration of the transport of Cerenkov photons along a direct line of sight through a core's coolant channels, the conditions under which refueling occur are different than those present during operation. Offline reactor inspection is an established procedure and is not the focus of this research effort.

The potential impact of this method is the addition of a new, non-invasive, low-footprint form of instrumentation to characterize in-core conditions in nuclear reactors during operation. Many instrumentation methods measure a small number of locations in or near the core to obtain the total core power. Some next generation reactor designs could benefit from improved power profile determination. Reactor designs that use an optically transparent coolant with straight coolant channels are the most likely candidates for the use of visual instrumentation. Unlike gamma and neutron detectors, the light sensors can be located far outside of the active core region, and thus can avoid many of the issues with radiation that are present in most other forms of instrumentation. The visible light power measurements should be valid in the intermediate to full power range.

This information could be used to measure flux tilts from xenon oscillations, temperature irregularities, rods in shifted positions, blocked channels or other phenomena. In some cases, it would be possible to localize the disturbance to which region of the reactor and possibly even which assembly or coolant channel(s). This can provide operators with more information about what the cause of an issue may be. A large amount of measureable information about the power profile in a reactor could also be used to validate reactor physics codes and models.

2. Cerenkov-based analysis methodology

2.1. Production, transport and detection of Cerenkov radiation

This method gathers information about the spatial power profile of a reactor by observing the amount of visible Cerenkov radiation coming out of the coolant channels or other coolant containing regions, such as inter-assembly spaces. Either a single

multichannel photon detector or an array of photon detectors can be placed some distance above the core to observe the Cerenkov production in each channel.

The Cerenkov light above the core is caused by the Cerenkov production within a channel, which is directly proportional to the electron flux in the channel. The electron flux within a coolant channel is in turn proportional to the gamma flux within the channel. In an operating TRIGA reactor, the gamma flux in a coolant channel is primarily caused by the fissions in the surrounding fuel pins. The fission rate density in fuel is proportional to the neutron flux. Thus, the Cerenkov observed above a channel is an indication of the power density and neutron flux within the surrounding pins. A diagram showing the progression from neutron flux to Cerenkov detection is shown in Fig. 1. The only step in this diagram that involves a distance larger than a few pin pitch lengths is the transport of the visible Cerenkov photons through the coolant. The visible photon transport occurs in a straight line due to the wave nature of low energy light, so there is little information loss.

The general steady state photon transport equation can be seen in equation (1) (Wang and Wu, 2007):

$$\mathbf{s} \cdot \nabla \Psi_{\text{photon}}(\mathbf{r}, \mathbf{s}) = -\mu_t \Psi_{\text{photon}}(\mathbf{r}, \mathbf{s}) + \mu_s \times \int_{4\pi} \Psi_{\text{photon}}(\mathbf{r}, \mathbf{s}') P(\mathbf{s}', \mathbf{s}) d\mathbf{s}' + S(\mathbf{r}, \mathbf{s}), \quad (1)$$

where \mathbf{r} is the position vector in space, \mathbf{s} is the unit direction vector, $\Psi_{\text{photon}}(\mathbf{r}, \mathbf{s})$ is the photon flux at point \mathbf{r} in direction \mathbf{s} , μ_t is the attenuation coefficient (similar to the total macroscopic cross section), μ_s is the scattering coefficient, $P(\mathbf{s}', \mathbf{s}) d\mathbf{s}'$ is the probability of a photon with direction \mathbf{s}' within $d\mathbf{s}'$ scattering into unit solid angle around direction \mathbf{s} , and $S(\mathbf{r}, \mathbf{s})$ is the spatially and angle dependent photon source term. The medium in which the photons are propagating and being produced is assumed homogenous.

For Cerenkov photons, the photon source term $S(\mathbf{r}, \mathbf{s})$ can be approximated by equation (2):

$$S(\mathbf{r}, \mathbf{s}) = \frac{1}{4\pi} \int dE' \Phi_{\text{Electron}}(\mathbf{r}, E') \Sigma_{\text{Cerenkov}}(E'), \quad (2)$$

where $\Phi_{\text{Electron}}(\mathbf{r}, E)$ is the spatial and energy dependent scalar electron flux. The quantity $\Sigma_{\text{Cerenkov}}(E') dE'$ is the energy dependent macroscopic cross section for Cerenkov production by electrons, equal to the number of Cerenkov photons produced by electrons with energies in dE' around E' per unit path length. This approximation adds the assumption that the electron flux is isotropic.

To find the Cerenkov flux at a specific point \mathbf{r} with photons within an angle range $d\mathbf{s}$ of a specified direction \mathbf{s} , a solution to some form of equation (1) must be obtained. This flux only depends on photons produced or scattered in the region contained by a cone of angle $d\mathbf{s}$ opening away from the point \mathbf{r} in the direction $-\mathbf{s}$. Viewing a coolant channel from a significant distance above the core provides a very small angle view of a thin, constant width region that produces Cerenkov photons. In such a situation where the angle range $d\mathbf{s}$ is small and the cross sectional area of the region contributing to the flux is both small and constant, this can be approximated by a line integral starting at \mathbf{r} in the direction of $-\mathbf{s}$. This is a simplification and solution of equation (1) as seen in equation (3):

$$\Psi_{\text{photon}}(\mathbf{r}, \mathbf{s}) = \int_0^\infty \left[\int_{4\pi} \Psi_{\text{photon}}(\mathbf{r} - r\mathbf{s}, \mathbf{s}') P(\mathbf{s}', \mathbf{s}) d\mathbf{s}' + S(\mathbf{r} - r\mathbf{s}, \mathbf{s}) \right] \frac{e^{-\mu_t r}}{r^2} dr. \quad (3)$$

The variable r (not bold) represents the distance from the point \mathbf{r} . The $\exp(-\mu_t r)$ term accounts for attenuation, while the $1/r^2$ term is for the dissipation over distance from a point source.

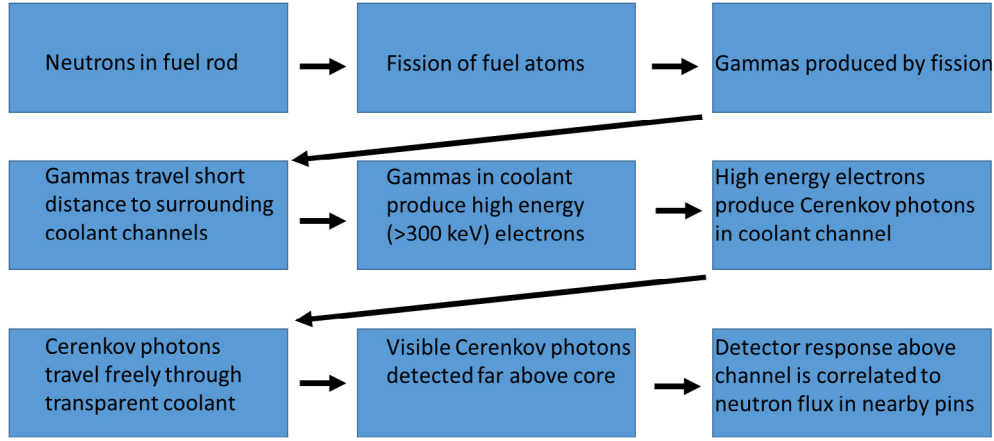


Fig. 1. Progression from neutrons in the fuel to Cerenkov detection above core.

The Cerenkov photons being detected have wavelengths in or very near the visible range, where light behaves less like a particle. The scattering of visible photons is relatively small, so an approximation is made such that the scattering of visible photons into the angle range is neglected as a source of photons contributing to the flux, and is only accounted for as part of the attenuation term, μ_t . This allows the scattering term in equation (3) to be dropped, leaving only the source term, the attenuation and the $1/r^2$ dependence. Inserting equation (2) into equation (3), applying the aforementioned approximations yields equation (4):

$$\Psi_{\text{photon}}(\mathbf{r}, \mathbf{s}) = \int_0^\infty dr \frac{1}{4\pi} \int dE' \Phi_{\text{Electron}}(\mathbf{r} - \mathbf{r}\mathbf{s}, E') \Sigma_{\text{Cerenkov}}(E') \frac{e^{-\mu_t * r}}{r^2}. \quad (4)$$

This can be approximated by a discretization that slices the region where significant contributions to the Cerenkov flux are made into segments and separating the energy dependent electron flux into bins. Doing this yields equation (5):

$$\Psi_{\text{photon}}(\mathbf{r}, \mathbf{s}) = \frac{1}{4\pi} \sum_{n=1}^{E \text{ bins}} \sum_{m=1}^{Segments} \Phi_{\text{Electron}}(z_m, E_n) \Sigma_{\text{Cerenkov}}(E_n) \frac{e^{-\mu_t * r_m}}{r_m^2}. \quad (5)$$

Another simplification is made that combines the $1/4\pi$, the Cerenkov production term, the exponential attenuation and the $1/r^2$ term into a single Cerenkov response function. This response function is a correlation between the electron flux in a bin and the amount of Cerenkov light that reaches the detection point. The response function is very similar to a cross section, because it is the amount of Cerenkov detected at the detection point per unit of electron path length in the specified region of the channel. Adding this simplification transforms equation (5) into equation (6):

$$\Psi_{\text{photon}}(\mathbf{r}, \mathbf{s}) = \sum_{n=1}^{E \text{ bins}} \sum_{m=1}^{Segments} \Phi_{\text{Electron}}(z_m, E_n) \Sigma_{\text{Response}}(z_m, E_n), \quad (6)$$

where Σ_{Response} is the aforementioned response function.

The determination and verification of the response cross sections is described separately in (Hearne and Tsvetkov, 2019) and (Hearne and Tsvetkov, 2020). Eq. (6) and the correlation factors are used to determine the amount of Cerenkov detected above the core without requiring the computationally expensive and potentially problematic simulation of Cerenkov photons in the whole core.

2.2. Modelling Cerenkov in TRIGA

MCNP 6.1.1 Beta is the primary tool used to model the reactor. This version of MCNP has the added capability to model photons with energies in the visible range, the use of indices of refraction, and the ability to produce and track Cerenkov radiation (Goorley, 2014). The Cerenkov production is governed by a discretized form of the Frank Tamm formula shown in equation (7): (Durkee and James 2013)

$$N = 2\pi\alpha L z^2 \sum_{i=1}^I \left(\frac{1}{\lambda_i} - \frac{1}{\lambda_{i-1}} \right) \left(1 - \frac{1}{\beta_i^2 n_i^2} \right). \quad (7)$$

Here N is the number of photons emitted, α is the fine structure constant, L is the total path length, λ is the wavelength, β is the ratio of the charged particle's speed to the speed of light and n is the frequency dependent index of refraction. Los Alamos has done verification of the Cerenkov production in MCNP 6.1.1 Beta to ensure that it does correctly produce the number of photons predicted (Durkee and James 2013).

In this research effort, methods that directly produce, track and tally Cerenkov photons in a model of the reactor are used, as well as methods that only track neutrons, gammas and electrons and rely on correlations to estimate the resulting Cerenkov fluxes. A model of the TRIGA has been developed to use in the Cerenkov analysis. A horizontal cross section of the core from the model can be seen in Fig. 2. The aqua colored background is water. The green blocks in the left and right portions of the picture are

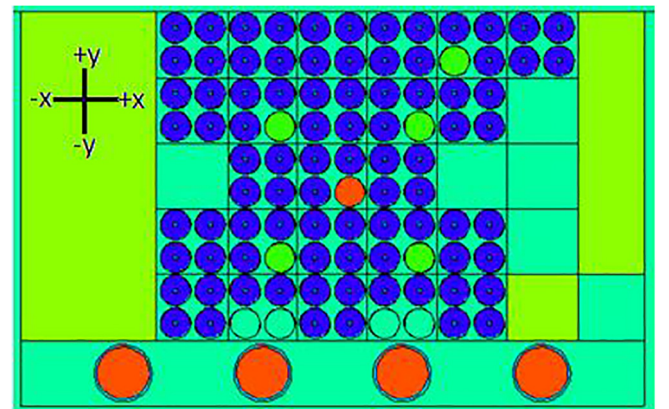


Fig. 2. Horizontal (XY) cross section of the TRIGA core with a directional compass.

graphite reflector blocks. The blue circles are the standard fuel pins. The green circle near the right side of the 2nd row is the regulating rod, the 4 other green circles are the safety shim control rods. The orange circle in the middle of the core is the transient control rod. The four large orange circles at the bottom of the picture are hollow chambers used for sample irradiations and other experiments.

This model was created without using any universe or lattice structures, due to an issue with refraction in MCNP 6.1.1 beta that causes lost particles when multiple universes are present. As is, each pin and structure is defined individually, with its own unique surfaces and cells. The reactor is oriented with the z axis corresponding to the vertical axis of the core and the $+y$ direction corresponding to the side of the reactor facing the graphite coupler box. The cells and surfaces for the pins and control rods are numbered based upon which position in the lattice they occupy. The general system for surface and cell designation used is AYYXXBB, where A and BB are used to denote what the cell or surface is, such as fuel meat, cladding, a top cap, etc. In many of the pin specific cells, digit A is not included; it is primarily used for denoting different water regions, and BB may only contain one digit for the first 9 cells. The digits for BB generally indicate which radial region of a fuel pin the surface or cell involves, such that 1 is cylinder bounding the inner zirconium rod, 2 is the fuel bound, 3 is cladding, etc. The digits for XX denote the x position of the cell in the lattice, while YY denotes the y position. For example, the 4th pin in the 3rd row is denoted as pin 3,4. The fuel region in this pin is cell 03042, where the 2 denotes the 2nd radial region of the pin. 03041 is the central zirconium rod.

The reactor model contains 86 regular fuel pins filling some of the locations in a 12×10 lattice. Each fuel pin was modeled with a zirconium rod in the center, surrounded by the Zr-H fuel, with stainless steel cladding. Graphite regions are placed axially above and below each fuel pin within the cladding and aluminum caps are at the top and bottom of each pin. There are four safety shim control rods in the (4,4), (4,8), (8,4), and (8,8) locations in the core. The safety shims are moveable rods that consist of a fuel region similar to the fuel pins with a boron carbide absorber region above it. The safety shims are fuel following to increase their reactivity worth, and are used to make large reactivity adjustments in the core. A vertical cross section of the 4th row of pins, showing fuel rods and two of the safety shims can be seen in the left side of Fig. 3. The transient control rod is located in the center of the core

at location (6,6). This is modeled as a moveable cylinder of boron carbide with aluminum endcaps within stainless steel cladding with air regions above and below it. The length of the boron region is the same as that of the fuel pins. When the transient rod is moved, the boron region with its caps moves within the air region, while the rest of the rod remains in place. The transient rod extends above the fueled region of the core such that when the transient rod is withdrawn the bottom of the absorber is slightly above the top of the fueled regions of the fuel rods. A vertical cross section of row 6, displaying the transient rod at full withdrawal can be seen in the middle section of Fig. 3. The regulating rod is a moveable control rod at location (2,9) in the second row of fuel pins. This control rod is not fuel following and is located near the periphery of the core so that it has a lower total reactivity worth. The regulating rod is primarily used for small reactivity changes and is usually adjusted automatically to regulate the reactor power and maintain it at a set level. The position designation of control rods ranges from 0 cm when fully inserted to 40 cm when fully withdrawn.

The core has graphite blocks beside it in the $+x$ and $-x$ directions that act as reflectors. In this model, they are approximated as continuous rectangular prisms without anything but graphite inside of them. The lower grid plate and the structures by which the pins are supported by the plate were approximated as a solid aluminum block with a few simple square and cylindrical holes in it for control rods and other tubes and instruments. The four irradiation tubes next to the core in the $-y$ direction are also modeled as cylinders of air with steel cladding. Due to the way that MCNP calculates geometries and transports particles, cells with large numbers of bounding surfaces can drastically increase runtime, so it was necessary to place planes to divide the water regions in the core into smaller regions that each contained only 4 pins to reduce the runtime.

One of the primary sources of error in the criticality estimation in this model is the usage of a single homogeneously burned and heated material for all of the fuel pins. Differences in the modeling of the materials and regions inside of the graphite block on the $-x$ side of the core also contribute to a difference in the k -eff estimates produced by this model. The higher fidelity lattice-based neutron-only input deck provided by the A&M Nuclear Science Center with many separately depleted zones in each fuel pin and a more detailed treatment of the graphite source region is used when more precise criticality estimates are needed. The more complex deck cannot be used for Cerenkov production due to the lattice lost

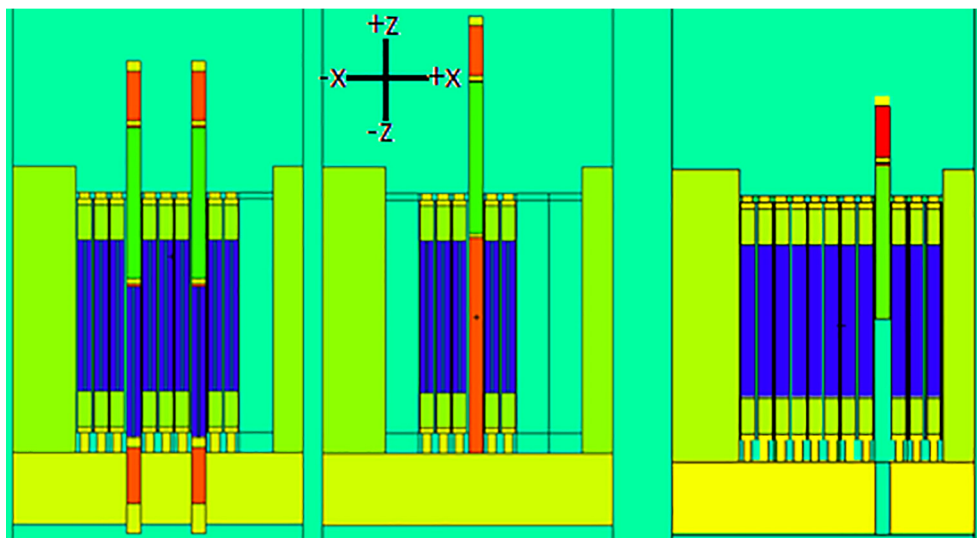


Fig. 3. Vertical (XZ) cross sections of row 4 (left) and row 6 (middle) and row 2 (right) displaying fuel pins, safety shims, the transient control rod, and the regulating rod.

particle issue. Use of the complex deck for gamma and electron fluxes is avoided due to computational constraints. Using the neutronics only model, the reactor is critical with the transient rod fully withdrawn, the safety shims withdrawn 28.4 cm and the regulating rod withdrawn by 19.8 cm. Modeling the reactor with these rod positions in the Cerenkov compatible model produces a k-eff estimate of 1.00556 ± 0.00037 . This degree of deviation, while significant from an operational standpoint, is acceptable for the modeling of Cerenkov fluxes, as MCNP will run the number of neutrons specified when using a kcode regardless of the actual criticality value. There is difference of nearly 1\$ of reactivity, but the number of photons produced is proportional to the number of fissions, and should only differ by 0.5%. Due to this discrepancy, the more accurate lattice based model with heterogeneously burned fuel is still used for determining different critical rod positions, which are then used in the simpler, lattice free model for modelling photons and electrons.

2.3. Two dimensional Cerenkov mapping

The spatial power profile information is primarily obtained by making a 2D map of the Cerenkov radiation coming from the coolant channels in the reactor. Due to the irregular and asymmetric nature of the reactor, some periphery coolant channels are not tallied, but instead a 9×9 grid of coolant channels is used for the investigation. All of the fuel pins in the reactor, as well as one of the graphite reflector blocks can be seen in Fig. 4 along with additional notations for the location of control rods and the electron tallies used for the Cerenkov response estimations. The safety shims are marked “Shim”, the transient control rod marked “TR” and the location of the regulating rod marked “RR”. The small circles between the pins are the portions of the coolant channels that are tallied. The red box shows the extent of the area covered by the Cerenkov map. The 4 pins in the top right corner of the reactor are excluded from the map to keep a rectangular region while avoiding having to deal with the presence of the graphite block at the bottom right corner. The coolant channels that border the left edge of the reactor are similarly excluded to avoid overlap between the cylindrical region being tallied and the graphite reflector. Those bordering the +y direction face of the core are excluded to avoid graphite/channel overlap issues when the coupler is close to touching the core. The bottom face is left out to maintain a more symmetrical arrangement with a square 9×9 grid.

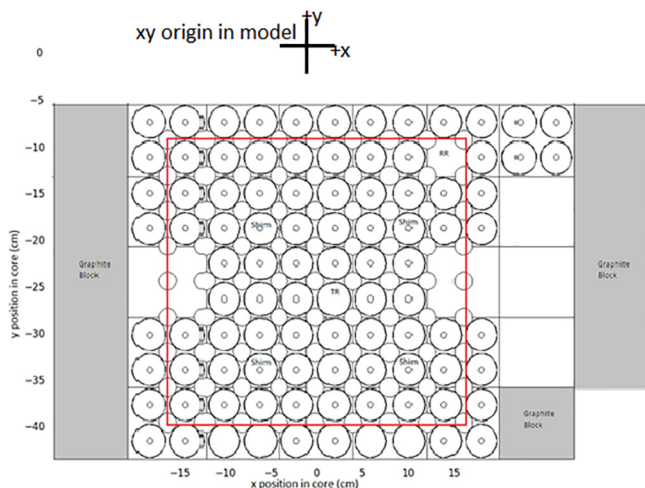


Fig. 4. XY cross section of core showing coolant channels tallied for Cerenkov map and control rod positions. The red box corresponds to the region that is mapped in the subsequent power profiles. (For interpretation of the references to color in this figure legend, the reader is referred to the web version of this article.)

A set of correlation factors, which are a discretization of $\Sigma_{\text{Response}}(Z_m, E_n)$, from equation (6) are used as a response function to correlate the electron flux tallied within a coolant channel to the Cerenkov flux detectable 2 m above the core. The correlation factors were produced using a separate set of input decks as described in (Hearne and Tsvetkov, 2019) and (Hearne and Tsvetkov, 2020) as part of the larger research effort. For a single coolant channel, the response function has the Cerenkov flux resulting from electrons in 23 energy bins ranging from 200 keV to 10 MeV and 16 spatial bins covering the height of the core.

The correlation factors are used to calculate the total Cerenkov response for each coolant channel. In MCNP, the electron flux in each channel is tallied and binned by energy and axial position, and then each bin is multiplied by its correlation factor to determine its contribution to the total Cerenkov response. Then all of the bins' Cerenkov contributions for a given channel are added together to obtain an estimate of the total Cerenkov flux that would be observed above that channel within the specified angle range. A block diagram illustrating how this process is used to produce the 2D map can be seen in Fig. 5.

Each of the 81 tallied coolant channels have 23 energy bins and 16 spatial bins for the electron flux within the channel. These 29,808 tally bin results are extracted and used with the response function to produce 81 total Cerenkov fluxes. Though the relative uncertainties for individual electron flux bins are high, the uncertainty for the total Cerenkov in a channel is usually very low, due to uncertainty propagation. The resulting Cerenkov flux in each of the 81 tallied coolant channels is plotted as a 2D map with a geometry overlay shown in Fig. 6. The large circles with very small circles inside them are fuel rods, while the small circles between the fuel rods are the regions of the coolant channels tallied for the electron fluxes.

This is a smeared estimate of the core's 2D power profile, as approximately 60% of the Cerenkov flux coming from each channel is caused by the 4 pins surrounding the channel, and 88% comes from the nearest 16 pins (Hearne and Tsvetkov, 2019). The advantage of this power profile estimate is that it can be obtained relatively easily, and does not require placing 81 detectors within the core, but could involve a single camera type detector using redirection through mirrors, lenses, or fiber optic cables, or using correction factors for the shadowing effects of channels not directly below the detector. The mirrors, lenses or fiber optic cables could re-direct the light from above each channel to a single multichannel photon detector, with the light from each coolant channel being detected by a different channel on the detector. The use of correction factors for shadowing could allow estimates of the total Cerenkov directly above a channel to be made by multiplying the flux at the detector by a factor based upon what portion of the channel is visible to account for the shadowing effect. It could require more than one detector depending on how far away from the core the detection plane is and the size of the core, but still far less than one detector per channel. The limiting factor is

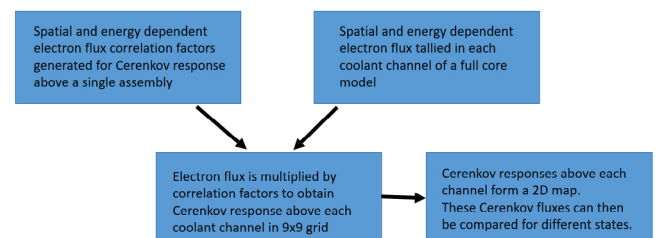


Fig. 5. Block diagram showing the method used to produce 2D Cerenkov maps above core from MCNP model.

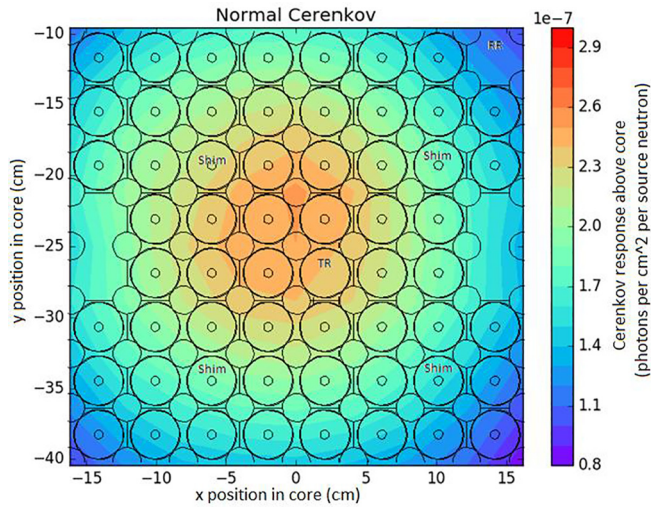


Fig. 6. This plot shows the Cerenkov estimates 2 m above the core, with and outline of the XY geometry of the core overlaying the image. The safety shims, transient rod (TR) and regulating rod (RR) positions are labeled. In this figure, the reactor is in the normal baseline critical state, with the regulating rod at 19.8 cm, the shims at 28.4 cm and the transient rod fully withdrawn. This is used as a baseline to compare with other perturbed reactor states. The scale of the plot is the normalized Cerenkov flux per fission neutron.

whether or not the detector has sufficient line of sight to the channel to give an accurate estimate of the Cerenkov produced in the channel without introducing unacceptable errors. If a view that at least reaches to the bottom of the channel is required, then at 2 m above the TRIGA reactor, nine detectors should be sufficient to get an accurate determination of the Cerenkov map without requiring any additional light redirection. A single detector or camera could be used if placed at least 6.5 m above the midplane, which is still below the surface of the pool located approximately 8 m above the midplane. Using a different height above the core for the detector will change the field of view for channels not directly below the detector, and will change the amount of light reaching the detector from the channel, due to the $1/r^2$ dependence for light intensity as a function of distance, and the exponential attenuation of the light caused by absorption in the water. A detector position of 2 m above the core midplane is used for this analysis. If a height other than 2 m were used, either the response functions could be generated again for the new height, or a correction factor based upon the different distance could be applied.

In Fig. 7, a graphic depicting the placement of either an array of detectors, or a single detector is shown. A simple experiment could be performed with a setup similar to the right side, using a single camera positioned far above the core, such that the angle between each channel and the viewpoint is still close enough to vertical for a sufficient portion of the channel to be visible. The models use a setup similar to the left side, with many detectors, using an assumption that the Cerenkov flux is observed directly above each channel. While this may be impractical in a real situation, the idealization makes the calculation of the Cerenkov fluxes simpler by not requiring various different corrections for shadowing effects, and allows the data to be more directly used to produce a flux map. For attempts at experimental verification, a single camera positioned far above the core, similar to the right side of Fig. 7, would be more likely, as this would be easier and less expensive to set up.

The values of each point in the 2D power profile scale linearly with reactor power. The full core power level is used as a normalization factor in the models that produce the 2D profiles. Therefore,

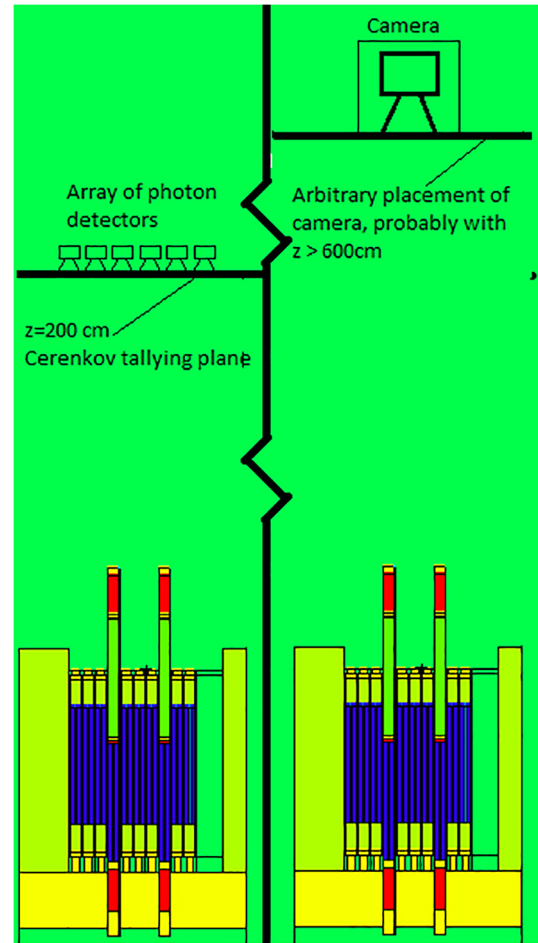


Fig. 7. Two possible ways to measure the Cerenkov flux above the core. An array of photon detectors (left) or a single, multichannel detector or camera (right).

a system that measures the power profile is also taking measurements from which the reactor power can be determined. This has been demonstrated experimentally elsewhere (Arkani and Gharib, 2007; Arkani and Gharib, 2009). As the total reactor power simply involves a scaling factor for the models used here, the focus of this research effort is on spatial effects.

2.4. Reactor state change analysis with 2D Cerenkov maps

One of the main metrics of the Cerenkov detection system is its ability to detect and identify perturbations in the reactor relative to a baseline, “normal” state. Various alterations to the state of the reactor are analyzed, all maintaining criticality with the same fuel temperature and power level. As the total power in the core remains constant, the observable changes will be in the power tilts and the power in specific regions of the reactor relative to others.

Due to the uncertainties in Monte Carlo simulations, relatively large changes in the reactor are investigated, to ensure that the differences are noticeable amid the noise. K-eff in the model used is approximately 1.006 for the normal critical state. This is slightly higher than 1 because the homogenization of the fuel burnup provides an increase in reactivity, but in the more complex, neutronics only model, the rod positions used to bring k-eff to 1. In this baseline case, the shims are withdrawn 28.4 cm and the regulating rod withdrawn 19.8 cm. This is the “normal” reactor state that is used as a comparison for the analysis of the perturbed states. In the altered reactor states, the safety shims are readjusted to maintain

the same level of criticality in the reactor, with the model's k-eff estimate again being close to 1.006. An alteration that inserts negative reactivity will thus have the safety shims slightly withdrawn to provide enough positive reactivity to counteract the change. This leads to an effect where a change in the power at one location causes a small opposite change throughout the rest of the core. To maintain consistency between different comparisons, the same scale is used for all Cerenkov map plots, absolute difference plots and relative difference plots. This causes some effects to be harder to distinguish in some plots, but the usage of both absolute and relative flux comparisons helps to circumvent this issue.

The first state change analyzed is the partial removal of the regulating rod, located near the edge of the reactor. The regulating rod is moved from close to 50% withdrawal at 19.8 cm to 40 cm, corresponding to a 100% withdrawal. The safety shims undergo a slight insertion to compensate, moving from 28.4 cm to 26.9 cm to maintain a close approximation of criticality. The estimates of the observable Cerenkov flux above the core in each coolant channel for the two states are subtracted from one another. For each channel, the difference is calculated using equation 8:

$$\text{Perturbed flux} - \text{baseline flux} = \text{absolute difference.} \quad (8)$$

Plotting the difference for each channel allows the effects of the perturbation to be seen more easily. In Fig. 8, the absolute difference plot for the case with the regulating rod withdrawn can be seen. The removal of the regulating rod and slight insertion of the shims causes a small decrease in the power in the lower left portion of the plot, as seen by the light blue region. The red region near the regulating rod corresponds to an increase in the Cerenkov observed in that area, caused by an increase in the neutron flux and fission rate, due to the removal of an absorber. The effect is hardly visible in this plot, because the absolute change in Cerenkov is being plotted, and the primary location of the change is at the periphery of the core, where the flux is lowest. A second difference plot, showing the relative difference of each channel is also produced, using equation (9):

$$\frac{\text{Perturbed flux} - \text{baseline flux}}{\text{baseline flux}} = \text{relative difference.} \quad (9)$$

The relative difference plot can be seen in Fig. 9. Analyzing the relative difference makes the change in Cerenkov production near the regulating rod very apparent. The four coolant channels in the

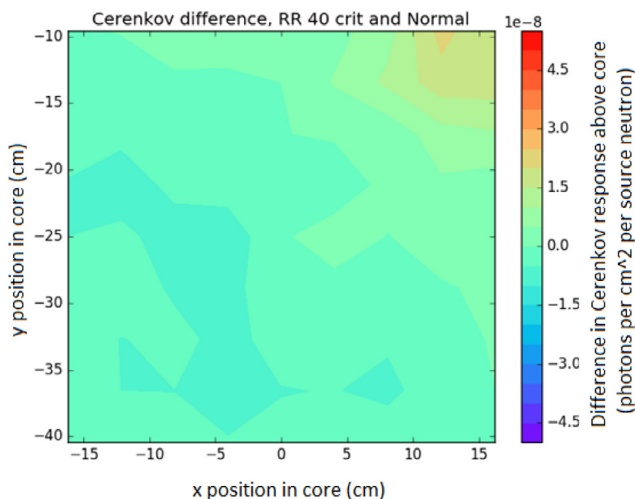


Fig. 8. Absolute difference in Cerenkov above the core comparing the reactor with the regulating rod fully withdrawn to the baseline case with the regulating rod close to 50% withdrawal.

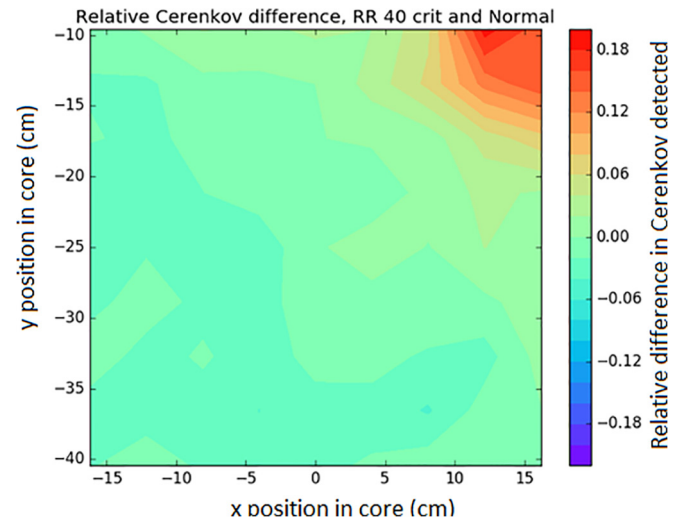


Fig. 9. Relative difference in Cerenkov above the core comparing the reactor with the regulating rod fully withdrawn to the baseline case with the regulating rod close to 50% withdrawal.

top right corner border the regulating rod, so as expected, that is where the change is the most significant. A smaller increase in the rest of the top right quadrant of the diagram is also evident due to the increase in the neutron flux.

The second comparison case modeled has the transient control rod near the middle of the reactor inserted to 20 cm, corresponding to a 50% withdrawal from the reactor, compared to the base state with a 100% withdrawn transient rod. The negative reactivity introduced by the transient rod insertion is counterbalanced by the almost complete removal of the shims to 36.8 cm, or 92% withdrawal. Any further insertion of the transient rod would not allow the reactor to maintain criticality with the same power level and fuel temperature. The transient rod is kept fully withdrawn during normal steady state reactor operation, and is primarily used when the reactor is operating in pulse mode. A partial insertion of the transient rod when the reactor is at full power is an unusual situation, but it is physically possible and provides some interesting flux shifts. A plot of the absolute difference in the Cerenkov radiation above the core caused by inserting the transient rod can be seen in Fig. 10, and the relative difference can be seen in Fig. 11.

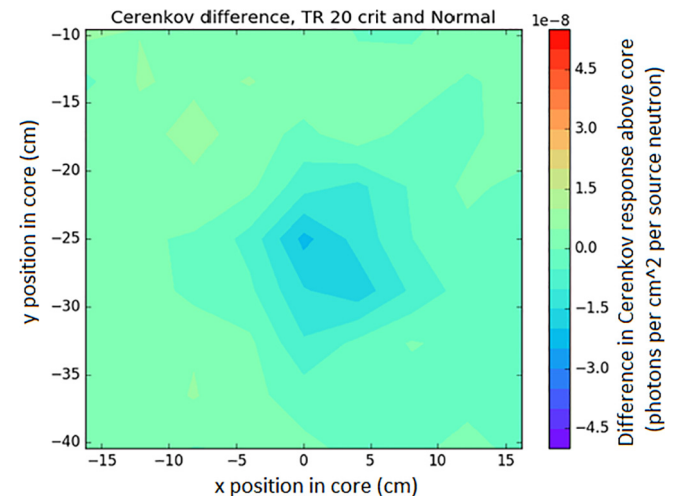


Fig. 10. Absolute Cerenkov difference when inserting the transient rod to a position of 20 cm.

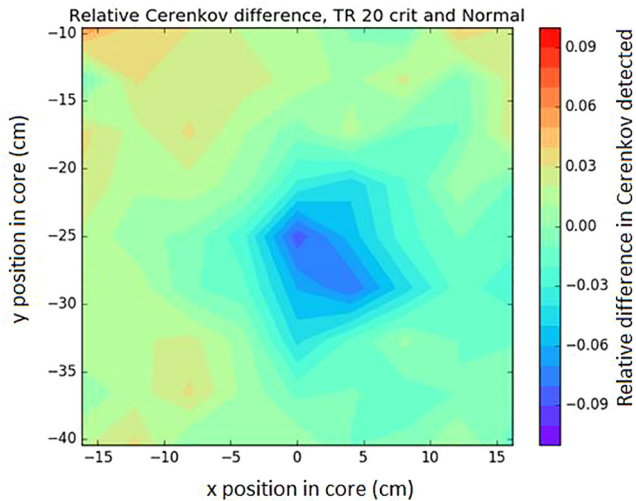


Fig. 11. Relative Cerenkov difference when inserting the transient rod to a position of 20 cm.

A large flux decrease can be seen in the middle of the core. The point where the magnitude of the drop is greatest corresponds to the coolant channel above and to the left of the transient rod in the reactor map, with the other three channels bordering the rod making up the rest of the bluest region on the plot. This depression in the flux is to be expected, and the ease with which the difference can be noticed in the estimated Cerenkov observations shows potential for its use as an additional method for detecting power shifts.

The third state change analyzed is the movement of the reactor next to the graphite coupler box. The +y direction face of the reactor is normally some distance away from the graphite box, such that the water between them is the only thing meaningfully affecting the reactor physics. The reactor can be moved within the pool to come very close to the coupler box so that neutrons from the core can diffuse into the coupler and down the neutron beam ports that are attached to it to be used for neutron radiography or other experiments. Changing the boundary condition of that face of the

core from water to graphite has a large effect on the reactivity and the flux distribution in the core, because the graphite absorbs less neutrons and acts as a better reflector than open water. To balance the reactivity insertion, the safety shims are inserted to 17 cm, compared to the baseline position of 28.4 cm. A picture produced using the VISual Editor (VISED) program included with MCNP showing the core next to the coupler box can be seen in Fig. 12. A plot of the total Cerenkov flux with the reactor next to the coupler is shown in Fig. 13. The peak of the observable Cerenkov flux is in the vicinity of $y = -15$ to -20 , compared to the baseline Cerenkov map that has its peak in the -20 to -25 region. This corresponds to a shift of about one pin unit cell. This +y shift in the flux profile is present throughout the rest of the core as well, such that the bottom right portion of the plot has less Cerenkov flux than the minimum bound used for the plots.

The absolute and relative comparative plots for the movement of the core towards the coupler box can be seen below in Fig. 14 and Fig. 15 respectively. There is a very large change in the Cerenkov production at the top of the plot, near the interface with the coupler box. Due to the low initial flux in this region, some points in relative difference plot exceeds the 20% bound on the scaling used for relative difference plots. The blue spots in the bottom portion of the plots, around $y = -35$ cm and the small blue bumps in the line across the $y = -20$ cm region correspond to the channels near the safety shims, where the local flux depression is more pronounced. The general gradient from the top to the bottom of the plot shows the lateral tilt of the flux across the whole core; this result has potential for being more directly quantified using the spatial derivative of the flux either at specific points, or averaged through the whole core. The usage of many channels across the core can make overall lateral tilts more apparent and reduce the reliance on individual data points. The detection of axial flux tilts along the direction of observation using a modification of this Cerenkov based method is discussed in (Hearne and Tsvetkov, 2019) and another forthcoming publication.

A similar though less pronounced type of whole core tilt can occur in some large thermal reactors when there is unequal fission product buildup and burn off, causing a phenomenon referred to as Xenon oscillations. Xenon oscillations are a positive feedback mechanism where a region of the reactor that has an increase in

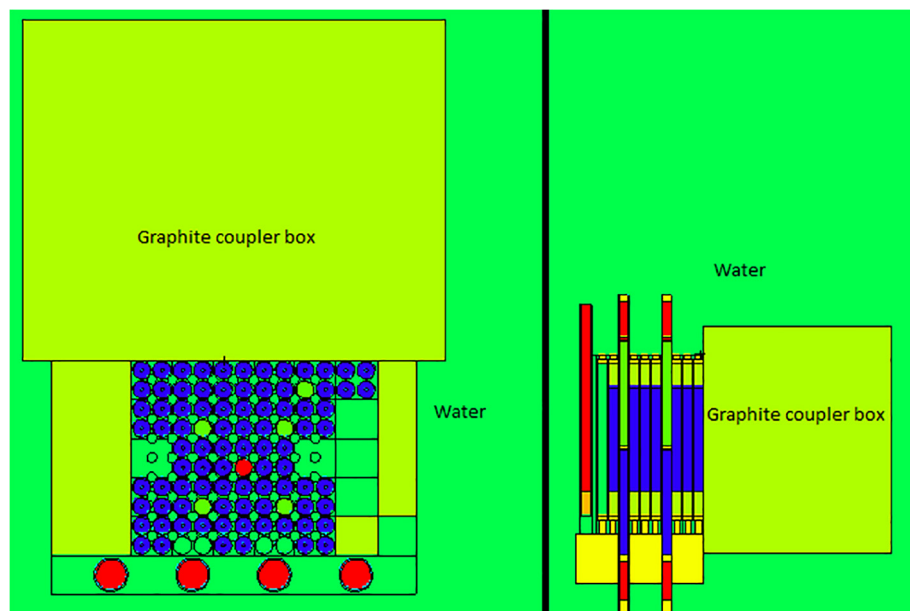


Fig. 12. Reactor core when moved next to coupler box, showing XY (left) and YZ (right) views of the core.

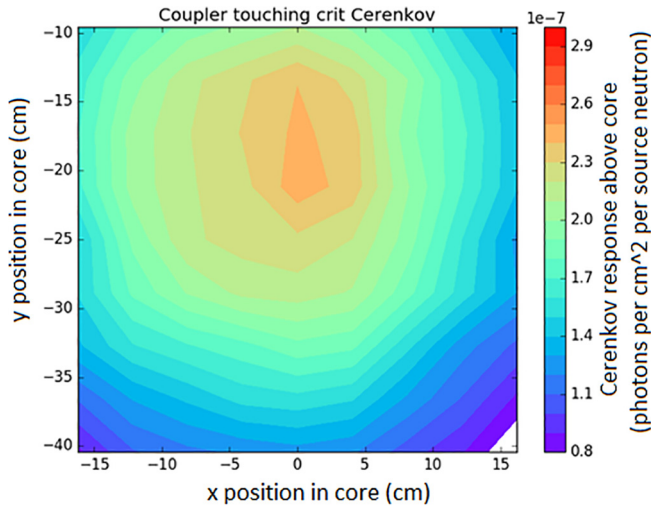


Fig. 13. Map of total Cerenkov above core with graphite coupler adjacent to core.

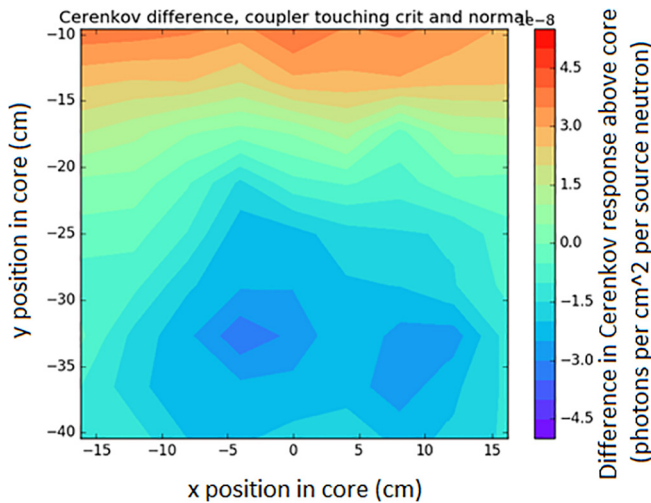


Fig. 14. Absolute Cerenkov difference when moving the core next to the graphite coupler box.

the flux starts to burn the highly absorptive indirect fission product Xenon-135 out faster than it is being produced from decay. This initially causes a further increase in the flux in that region, until the increased fission rate and production of Xenon 135 through the decay of Iodine-135 catches up, after which the Xenon levels in the fuel will increase beyond equilibrium, causing a decrease in the flux. These oscillations can lead to instabilities that require control actions and possibly early reactor shutdowns, a problem that has been studied extensively for large PWRs (Shimazu, 2004; Parhizkari et al., May 2015; El-Bassioni and Poncelet, 1974; Chernick et al., 1961) and other large thermal reactors (Shimjith et al., 2010). Early, accurate, detailed detection of flux shifts can allow action to be taken to mitigate such issues in a more effective manner.

3. Generalization of system for use in other reactor types

3.1. Reactor sensor calibration

To ensure accuracy, every reactor sensor must be calibrated in some way. Reactor sensor calibration for power monitors is initially done using the calorimetric method (Westinghouse 0000). In closed loop reactors, the calorimetric method obtains the reactor

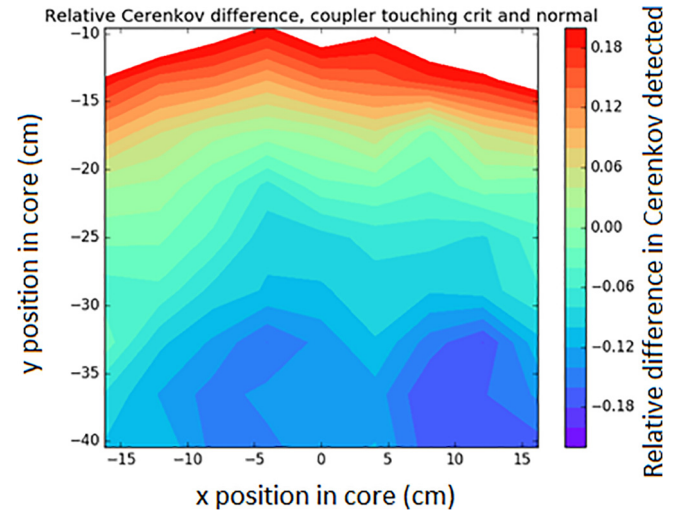


Fig. 15. Relative Cerenkov difference when moving the core near the coupler box. The white region at the top corresponds to a greater than 20% flux increase. The color scale is left unchanged so that this relative difference plot is consistent with the others.

power be observing the change in temperature of the coolant between the inlet and outlet of the core. This change in temperature, combined with the mass flow rate of coolant through the core and the heat capacity of the coolant gives the rate at which heat is being added to the coolant and thus the total reactor power. In some pool type reactors, the calorimetric method instead uses the change in temperature of the pool over time, first using electric heaters of a known power to affect a change, and then using the reactor to create a change in the temperature of the pool (Mesquita et al., 2007). The power obtained through the calorimetric method is then used to calibrate other power monitoring detectors by relating the output from the detectors to the known power level during the calibration.

Sensors must be periodically recalibrated to ensure that accuracy does not deteriorate over time. Historically, most sensor recalibration is done during refueling outages; efforts have been made to move towards online sensor calibration monitoring to reduce unnecessary recalibrations and shorten refueling and maintenance outages (Coble et al., 2012; Hashemian, 1995; Hines and Davis, 2005). Digital systems can be used to perform fault detection and diagnosis by comparing sensor outputs to previous data, redundant sensors of the same type, or to analytical predictions based upon other sensor types (Ma and Jiang, 2011; Bernard et al., 1984).

The calibration of a Cerenkov based power profile mapping system could be done in a similar way, thus relating the light detected to power measurements from other detectors. An additional system would provide more data to use in fault detection to further increase the reliability and to expand the types of faults detectable.

During the length of a fuel cycle, a reactor will also undergo changes based upon the burnup of the fuel, resulting shifts in the flux and power densities. The Cerenkov based power profile mapping could be re-calibrated periodically to update what the baseline state is based upon the reactor burnup. After refueling, the expected burnup dependent baseline could be used or compared to the new flux values at similar burnups in future cycles. Further modelling of the reactor with different burnups could also create expected Cerenkov fluxes at those burnups. By coupling measurements with burnup dependent models, the changes in the Cerenkov flux over time could potentially help to measure or validate the actual burnup in the core.

3.2. Applicability to LWR

A PWR is similar in some ways to the TRIGA reactor modeled here in that there are cylindrical fuel elements in a square lattice and the coolant is liquid water with no bulk boiling (Westinghouse 0000). However, there are some differences that present additional challenges for the usage of a Cerenkov based power-profiling system for an operating PWR. The fuel pins are much smaller in a PWR and the spacing between them is correspondingly smaller. The fuel pins are also longer than in the TRIGA, so the length to spacing ratio is substantially larger. Additionally, the grid plates that hold the fuel pins in place can hinder visual access to the spaces between the pins. There is also limited space above the fuel assemblies due to the top of the pressure vessel and the presence of the various structures within the vessel above the active core region, limiting how far above the top of the fuel that a visual instrumentation viewpoint can be placed. These factors put much tighter constraints on the lateral location of viewpoints above coolant channels. Locations other than coolant channels, such as control rod water holes or spacing between assemblies may provide a better line of sight through the core region to enable a Cerenkov based instrumentation method to be applied. The lack of vertical space above the fuel region could also cause the sensors to be in a stronger radiation field, due to the lack of shielding space between the fissions and the sensors. In general, the tight packing of a PWR and lack of additional space in the pressure vessel creates additional difficulty for the use of visual instrumentation, but there is still potential for it to be done.

Another concern is that the coolant within a PWR undergoes nucleate boiling during operation. The hot channels can have a maximum void fraction close to 1% (Westinghouse 0000). The presence of gas bubbles in water can significantly alter its reflectivity and transparency (Russell, 2010), which could cause significant changes in the amount of Cerenkov radiation reaching a sensor above the channel. If this were the case, the response in the sensor above the channel would fluctuate with the turbulent random nature of the fluid flow and would thus likely lose much of its value as a metric of power production. The effects of nucleate boiling on the transmissivity of the coolant would need to be investigated further before utilization of visual instrumentation in a PWR could be implemented. It is not expected that the effect of the turbulent flow of the liquid water will distort the collectable power profile data enough to prevent it from being used, but further investigation is needed to determine if this is the case.

A BWR would have a very significant problem with the boiling obscuring any line of sight through the core, and the moving bubbles causing a randomly fluctuating detector response. Therefore, a visual instrumentation system for online power monitoring in a BWR is not recommended.

Some small modular reactor designs (Liu and Fan, 2014) could be more easily fitted with visual instrumentation. The smaller core could more feasibly be covered by a single detector, and designs with additional space above the fuel assemblies could allow the detector to be outside of the stronger radiation fields.

3.3. Applicability to FHR

The Fluoride-Salt-Cooled High-Temperature Reactor (FHR) (C. Forsberg, L.-W. Hu, P. Peterson and K. Sridharan, "Fluoride-Salt-Cooled High-Temperature Reactor (FHR) for Power and Process Heat," Nuclear Energy University Programs, 2014; Scarlat et al., 2014; Brown et al., 2017) is a reactor design that could make use of Cerenkov based visual instrumentation for power profile determination (Holcomb et al., 2009). The primary salt considered as a coolant for the FHR is a Lithium-Beryllium-Fluoride (FLiBe) salt mixture with a 2 to 1 ratio of LiF to BeF₂; however, some of the

properties of FLiBe salt are still not fully characterized (Romatoski and Hu, 2017). Specifically, the optical properties and index of refraction for FLiBe salt are either not known or not publicly available. The optical properties of LiF salt are known; the index of refraction of solid LiF salt at room temperature for photons in the visible spectrum ranges from $n = 1.3996$ for 3.179 eV photons to $n = 1.3902$ for 1.771 eV photons (Palik and Hunter, 1997; Polyanskiy, 2019; Li, 1976). The Molten Salts Handbook lists the refractive index of liquid LiF at 950 °C as 1.32 (Janz, 1967). Refractive properties of BeF₂ salt are not available. FLiBe is 67% LiF salt and the refractive index of LiF is similar to the refractive index of liquid water, 1.333, so it is assumed that the refractive properties of liquid FLiBe salt will be similar enough to produce usable Cerenkov responses. Accurate modeling of Cerenkov production in FLiBe salt would require data for the refractive properties, which could be obtained experimentally if a Cerenkov based power-profiling system for an FHR is pursued.

The geometry of an FHR is not yet fixed, due to the reactor being in the design stage. There are various different geometries considered for the FHR using tristructural isotropic (TRISO) particle based fuel. Some versions of the design use hexagonal fuel elements consisting of graphite fuel plates with rectangular coolant channels between the plates (Ramey and Petrovic, 2018). In these designs, the coolant channels run the entire axial length of the fueled region core. If the channels extend beyond the fueled region to a location where a detector can be placed, a straight line of sight through the core would be possible, allowing for the visual instrumentation method developed here to be implemented. One other potential advantage of visual instrumentation in an FHR is that the presence of any frozen FLiBe salt in the coolant channels would cause noticeable disturbances in the light detector responses, similar to a coolant channel blockage by other debris. The ability to detect another potential operational issue is an added benefit. Solidified salt is not expected to be present in the core or coolant loop under normal conditions, so it would not normally interfere with the instrumentation.

3.4. Applicability to HTGR or other gas cooled designs

High Temperature Gas-Cooled Reactors, (HTGRs) (Moore et al., 1982) are reactor designs using TRISO (Demkowicz et al., 2018) particle fuel in a graphite matrix and helium gas as the coolant. Both prismatic fuel block (Liem and Sekimoto, 2008) and pebble bed fueled designs exist. There are many similarities between the FHR and HTGR reactor designs, with the coolant choice as the primary difference. Pebble bed designs would not be as viable for Cerenkov based power instrumentation, because the arrangement of the fuel pebbles would preclude a straight line of sight through the core, and shifting of pebbles would change the amount of light reaching a detector. Prismatic fuel designs with straight coolant channels do have some potential for utilizing visual instrumentation.

One issue is that the index of refraction of helium at atmospheric pressure is 1.000035, lower than that of most other gasses. This causes an increase in the required electron energy for Cerenkov production, as the electrons must have a velocity greater than c/n , which in this case is .999965c, corresponding to an energy of 60 MeV. No electrons of this energy are expected to be present in the coolant of a reactor, so if the density of the helium gas was the same as it is at standard temperature and pressure, there would be no Cerenkov production. However, the difference between the index of refraction of an ideal gas and 1 (the quantity $n-1$) is approximately proportional to the gas's density (Sang and Jeon, 2016; Michels and Hamers, 1937), and the helium gas in HTGRs is generally at a high pressure, so the refractive index will be higher. Of the various different HTGR designs used in the past,

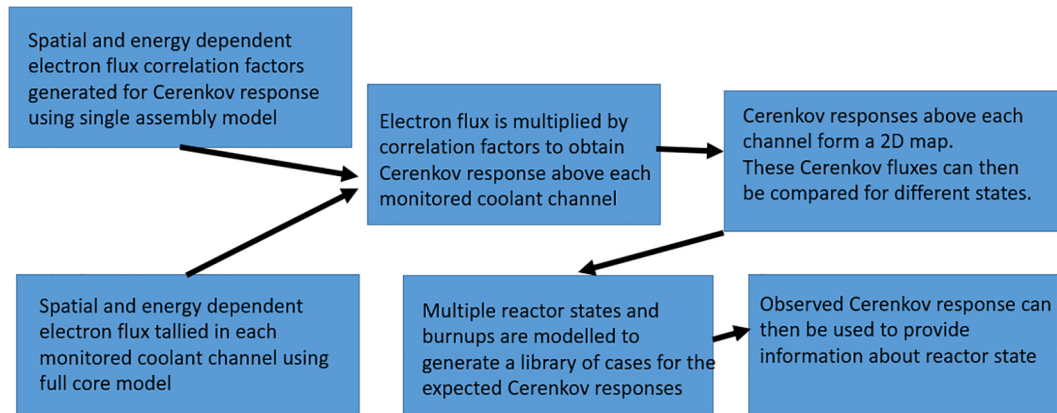


Fig. 16. Diagram of steps required to apply the modelling portion to a reactor.

typical values for the coolant pressure and average temperature are around 4 MPa and 600C (Mcdowell et al., 2011). In these conditions, the density of helium is 2.193 kg/m^3 , more than 12 times the density at STP. The estimated index of refraction at this density is 1.00044, which corresponds to a minimum electron velocity of .99956c and an energy of 16.7 MeV for Cerenkov production. This is still higher than the energy range of electrons produced by gamma interactions within the coolant of a reactor, so it is therefore expected that very little Cerenkov radiation would be produced in the coolant, preventing the use of this method for Cerenkov production based visual instrumentation in an HTGR.

3.5. Steps for implementation

The process for implementing this method in power profile reconstruction procedures is summarized below. On the physical side, a transparent coolant with a straight line of sight from the core to an external detection point is needed, likely through a coolant channel. Some form of photon detector that can survive the physical environment present at the detection point is needed. A transparent window of glass or some other material that can survive contact with the coolant at operating temperatures with chemically reacting would allow a detector to be somewhat insulated from the environment, though it will still likely be operating at a high temperature. The photon detectors can be installed at a number of locations, based upon the availability of locations and the desired resolution of the power profile map. A calibration of the responses from the photon detectors against other power measurement systems should also be done to accurately correlate the response to the power.

To implement the modelling portion of this method, a model of at least a coolant channel with a photon detector is needed to produce the correlation factors. The model can be run for a set of spatial and energy bins for the electron flux to relate the flux in the channel to a Cerenkov response above the channel. This is the portion that requires the production and tracking of Cerenkov photons in the model, so simplicity is ideal to avoid any issues with MCNP's treatment of low energy photons. A diagram summarizing this process can be seen in Fig. 16.

A whole core model is needed to model the power profile and obtain the predicted corresponding Cerenkov responses. This model needs to track neutrons, gammas and electrons, but does not need to explicitly model Cerenkov photons. The coolant channels that have photon detectors monitoring them should have electron tallies with a bin structure that matches up to the correlation factors. The results of the electron tallies can be combined with the correlation factors from the simple model to estimate the Cerenkov

flux detected by the photon detectors. For increased fidelity over changing burnups, versions of the whole core model at different burnups could be used to model how the Cerenkov flux above the core would change throughout the fuel cycle.

4. Conclusions

A method for determining the power profile with visual instrumentation in a reactor with an optically transparent coolant has been developed. The TRIGA reactor at Texas A&M is used as a surrogate case for any reactor with a transparent coolant. This method uses visible light detectors above the core to measure the Cerenkov radiation coming from coolant channels to provide information about the power density in the pins surrounding the channels. This can create a 2D map of the power density in the core, which has been demonstrated to detect changes in the power profile caused by changes in rod positions, coolant channel blockages, and changes in the position of the reactor within the pool. The total power from the reactor can also be measured using this system.

Further work to be done on developing this method is primarily in the direction of reactor specific application and designing the physical detection system. This research effort has been entirely model and theory based and has not yet been experimentally validated. To apply this to another reactor, a set of models of the reactor would need to be produced in a manner similar to what is done here. A physical system of photon detectors that can survive the reactor environment is necessary for this to be implemented; the experimental aspects of development have not yet been pursued. Additionally, the creation of a wider library of reactor states and their corresponding Cerenkov responses could be produced and some form of recognition software developed to automatically identify the reactor state based upon an observed Cerenkov response. Accounting for changing burnup would also increase the fidelity and applicability of the method.

Acknowledgements

This research is being performed using funding received from the DOE Office of Nuclear Energy's Nuclear Energy University Program, NEUP Award Number DE-NE0008306.

Disclaimer

This paper was prepared as an account of work sponsored by an agency of the United States Government. Neither the United States Government nor any agency thereof, nor any of their employees, makes any warranty, expressed or implied, or assumes any legal

liability or responsibility for the accuracy, completeness, or usefulness of any information disclosed.

Any views, opinions, findings, conclusions, or recommendations expressed in this publication are those of the authors and do not necessarily state or reflect the views of the Department of Energy Office of Nuclear Energy.

Appendix A. Supplementary data

Supplementary data to this article can be found online at <https://doi.org/10.1016/j.anucene.2019.107071>.

References

- Arkani, M., Gharib, M., Design and Construction of an Independent Channel for Tehran Research Reactor Power Measurement Using Cherenkov Detector, M. S. Thesis, Azad University, Research and Science Department, Tehran, 2007.
- Arkani, M., Gharib, M., 2009. Reactor core power measurement using Cherenkov radiation and its application in Tehran Research Reactor. *Ann. Nucl. Eng.* 36, 869–900.
- Bentoumi, G., Benson, B., Chan, P.K., Gaudet, M., Li, L., Samuleev, P., Sur, B., April 2018. Reactor power monitoring using Cherenkov radiation transmitted through a small-bore metallic tube. *Ann. Nucl. Energy* 114, 86–91.
- Bernard, J.A., Lanning, D.D., Ray, A., 1984. Digital control of power transients in a nuclear reactor. *IEEE Trans. Nucl. Sci.* 31 (1), 701–705.
- Brown, N.R., Betzler, B.R., Carbajo, J.J., Wysocki, A.J., Greenwood, M.S., Gentry, C., Qualls, A.L., 2017. Preconceptual design of a fluoride high temperature salt-cooled engineering demonstration reactor: core design and safety analysis. *Ann. Nucl. Energy* 103, 49–59.
- Chernick, J., Lellouche, G., Wollman, W., 1961. The effect of temperature on xenon instability. *Nucl. Sci. Eng.* 10 (2), 120–131.
- Coble, J.B., Meyer, R.M., Ramuhalli, P., Bond, L.J., Hashemian, H., Shumaker, B., Cummins, D., 2012. A Review of Sensor Calibration Monitoring for Calibration Interval Extension in Nuclear Power Plants. Pacific Northwest National Lab, Richland, WA.
- Demkowicz, P.A., Liu, B., Hunn, J.D., 2018. Coated particle fuel: Historical perspectives and current progress. *J. Nucl. Mater.*
- Durkee, J.W., James, M.R., rkee and James 2013. MCNP6 Cherenkov Radiation Feature Verification. Los Alamos National Lab, Los Alamos, New Mexico.
- El-Bassioni, A.A., Poncelet, C.G., 1974. Minimal time control of spatial xenon oscillations in nuclear power reactors. *Nucl. Sci. Eng.* 54 (2), 166–176.
- Farley, S., An overview of non destructive inspection services in nuclear power plants. In: *Proceedings of the International Conference Nuclear Energy for New Europe 2004*, 2004.
- Forsberg, C., Hu, L.-W., Peterson, P., Sridharan, K., Fluoride-Salt-Cooled High-Temperature Reactor (FHR) for Power and Process Heat, Nuclear Energy University Programs, 2014.
- Forster, J.J., 1965. In-core neutron flux instrumentation. *IEEE Trans. Nucl. Sci.* 12 (6), 8–14.
- T. Goorley, MCNP6.1.1-Beta Release Notes, Los Alamos National Lab, 2014.
- Hashemian, H., 1995. On-line testing of calibration of process instrumentation channels in nuclear power plants. Phase 2, Final report, NRC.
- Hearne, J.A., Tsvetkov, P.V., 2019. Spatial Power Profiling Method Using Visual Information in Reactors with Optically Transparent Coolants. (Ph.D. dissertation). College of Eng., Texas A&M University, College Station, Texas.
- Hearne, J.A., Tsvetkov, P.V., 2020. Response function generation for Cherenkov radiation production and transport in a TRIGA coolant channel. *Ann. Nucl. Energy* 138, 107200.
- Hines, J., Davis, E., 2005. Lessons learned from the U.S. nuclear power Plant on-line monitoring programs. *Prog. Nucl. Energy* 46 (3–4), 176–189.
- Holcomb, D.E., Cetiner, S.M., Flanagan, G.F., Peretz, F.J., Yoder, G.L.J., 2009. An Analysis of Testing Requirements for Fluoride Salt-Cooled High Temperature Reactor Components. Oak Ridge National Laboratory, Oak Ridge, Tennessee.
- Holcomb, D.E., Kisner, R.A., Cetiner, S.M., 2018. Instrumentation Framework for Molten Salt Reactors. Oak Ridge National Laboratory.
- Holschuch, T.V., Marcum, W.R., 2019. The CRANK System—A Simple, Robust Apparatus for Measurement of Cherenkov Light at Open-Pool Reactor. *Nucl. Tech.* <https://doi.org/10.1080/00295450.2019.1640515>.
- Janz, G.J., 1967. I.F – Refractive Index. In: *Molten Salts Handbook*. Academic Press, pp. 89–92.
- Knoll, G., 2010. Radiation Detection and Measurement. Wiley.
- Li, H.H., 1976. Refractive index of alkali halides and its wavelength and temperature derivatives. *J. Phys. Chem. Ref. Data* 5 (2), 329–528.
- Liem, P.H., Sekimoto, H., 2008. Small high temperature gas-cooled reactors with innovative nuclear burning. *Prog. Nucl. Energy* 50 (2–6), 251–256.
- Liu, Z., Fan, J., 2014. Technology readiness assessment of Small Modular Reactor (SMR) designs. *Prog. Nucl. Energy* 70, 20–28.
- Loving, J.J., 1970. Neutron, temperature and gamma sensors for pressurized water reactors. *IEEE Trans. Ind. Electron. Control Instrum.* 17 (2), 120–129.
- Lovvorn, J.L., Oct. 1961. Reactor power monitor utilizing Cherenkov radiation. *IRE Trans. Nucl. Sci.* 8 (4), 3–5.
- Ma, J., Jiang, J., 2011. Applications of fault detection and diagnosis methods in nuclear power plants: a review. *Prog. Nucl. Energy* 53 (3), 255–266.
- Mcdowell, B., Mitchell, M., Pugh, R., Nockolaus, J., Swearinged, G., 2011. High Temperature Gas Reactors. Pacific Northwest National Lab.
- Mesquita, A.Z., Rezende, H.C., Tambourgi, E.B., 2007. Power calibration of the TRIGA mark I nuclear research reactor. *J. Braz. Soc. Mech. Sci. Eng.* 29 (3), 240–245.
- Michels, A., Hamers, J., 1937. The effect of pressure on the refractive index of CO₂: the Lorentz-Lorenz formula. *Physica* 4 (10), 995–1006.
- Moore, R.A., Kantor, M.E., Brey, H.L., Olson, H.G., 1982. HTGR experience, programs, and future applications. *Nucl. Eng. Des.* 72 (2), 153–174.
- Palik, E.D., Hunter, W.R., 1997. Lithium fluoride (LiF). In: *Handbook of Optical Constants of Solids*. Naval Research Laboratory, Washington, D.C, pp. 675–693.
- Parhizkari, H., Aghaie, M., Zolfaghari, A., Minuchehr, A., May 2015. An approach to stability analysis of spatial xenon oscillations in WWER-1000 reactors. *Ann. Nucl. Energy* 79, 125–132.
- Polyanskiy, M., Refractive index database, [Online]. Available: <https://refractiveindex.info>. [Accessed 17 5 2019].
- Ramey, K.M., Petrovic, B., 2018. Monte Carlo modeling and simulations of AHTR fuel assembly to support V&V of FHR core physics methods. *Ann. Nucl. Energy* 118, 272–282.
- BWR Refueling Machine Camera N180-TZ. [Film]. Ahlberg Cameras, 2012.
- Rippon, S.E., 1963. Cherenkov detectors for the measurement of reactor power. *Nucl. Ins. Methods* 21, 192–196.
- Romatoski, R.R., Hu, L.W., 2017. Fluoride salt coolant properties for nuclear reactor applications: a review. *Ann. Nucl. Energy* 109, 635–647.
- Russell, S., 2010. Bright Water: Hydrosols, Water Conservation and Climate Change. Harvard, Cambridge, MA.
- Safeguards Techniques and Equipment 2011 Edition, Vienna: IAEA.
- Sang, B.H., Jeon, T.-I., 2016. Pressure-dependent refractive indices of gases by THz time-domain spectroscopy. *Optics Express* 24 (25).
- Scarlatt, R.O. et al., 2014. Design and licensing strategies for the fluoride-salt-cooled, high-temperature reactor (FHR) technology. *Prog. Nucl. Energy* 77, 406–420.
- Shimazu, Y., 2004. Simplest simulation model for three-dimensional xenon oscillations in large PWRs. *J. Nucl. Sci. Technol.* 41 (10), 959–965.
- Shimjith, S.R., Tiwari, A.P., Naskar, M., Bandyopadhyay, B., 2010. Space-time kinetics modeling of Advanced Heavy Water Reactor for control studies. *Ann. Nucl. Energy* 37 (3), 310–324.
- Wang, L.V., Wu, H.I., 2007. Biomedical Optics. Wiley.
- H. Weiss, Power measurement and automatic reactor control by gamme – or cerenkov – radiation, in *Nuclear Electronics*, Vienna, Austria, 1965.
- Westinghouse, AP1000 Design Control Document, NRC.
- Westinghouse, Westinghouse Technology Systems Manual, USNRC HRTD.